



UvA-DARE (Digital Academic Repository)

Host-guest tuning of the CO₂ reduction activity of an iron porphyrin cage

Surendran, Adarsh Koovakattil; Tripodi, Guilherme L.; Pluhařová, Eva; Pereverzev, Aleksandr Y.; Bruekers, Jeroen P.J.; Elemans, Johannes A.A.W.; Meijer, Evert Jan; Roithová, Jana

DOI

[10.1002/ntls.20220019](https://doi.org/10.1002/ntls.20220019)

Publication date

2023

Document Version

Final published version

Published in

Natural Sciences

License

CC BY

[Link to publication](#)

Citation for published version (APA):

Surendran, A. K., Tripodi, G. L., Pluhařová, E., Pereverzev, A. Y., Bruekers, J. P. J., Elemans, J. A. A. W., Meijer, E. J., & Roithová, J. (2023). Host-guest tuning of the CO₂ reduction activity of an iron porphyrin cage. *Natural Sciences*, 3(1), Article e20220019.
<https://doi.org/10.1002/ntls.20220019>

General rights


It is not permitted to download or to forward/distribute the text or part of it without the consent of the author(s) and/or copyright holder(s), other than for strictly personal, individual use, unless the work is under an open content license (like Creative Commons).

Disclaimer/Complaints regulations

If you believe that digital publication of certain material infringes any of your rights or (privacy) interests, please let the Library know, stating your reasons. In case of a legitimate complaint, the Library will make the material inaccessible and/or remove it from the website. Please Ask the Library: <https://uba.uva.nl/en/contact>, or a letter to: Library of the University of Amsterdam, Secretariat, P.O. Box 19185, 1000 GD Amsterdam, The Netherlands. You will be contacted as soon as possible.

RESEARCH ARTICLE

Host-guest tuning of the CO₂ reduction activity of an iron porphyrin cage

Adarsh Koovakattil Surendran¹ | Guilherme L. Tripodi¹ | Eva Pluhařová² |
Aleksandr Y. Pereverzev¹ | Jeroen P. J. Bruekers¹ | Johannes A. A. W. Elemans¹ |
Evert Jan Meijer³ | Jana Roithová¹ 

¹Institute for Molecules and Materials, Radboud University, Nijmegen, The Netherlands

²J. Heyrovský Institute of Physical Chemistry, v.v.i., The Czech Academy of Sciences, Prague, Czech Republic

³Van 't Hoff Institute for Molecular Sciences and Amsterdam Center for Multiscale Modelling, University of Amsterdam, Amsterdam, The Netherlands

Correspondence

Institute for Molecules and Materials, Radboud University, Heyendaalseweg 135, 6525 AJ Nijmegen, The Netherlands.
Email: j.roithova@science.ru.nl

Funding information

Netherlands Organization for Scientific Research, Grant/Award Numbers: 740.018.022, VI.C.192.044

Abstract

Efficient electrocatalytic CO₂ reduction requires developing catalysts with high selectivities and high activities, which is simultaneously difficult to achieve. Here, we present a new approach to tune the CO₂ reduction activity based on host-guest chemistry enabled by an iron porphyrin cage catalyst. The cage design allows the hosting of alkali metals in the side walls causing a change in the electrostatic potential inside the cage cavity. Density functional theory calculations show that the guest potassium ions assist the reduction of CO₂ by inverting the two-electron transfer from iron(0) to CO₂ from endothermic to exothermic. Accordingly, electrochemical experiments with the cage catalyst show that in the presence of the potassium ions, the overpotential for the CO₂ reduction decreases, and the catalytic activity increases while the high selectivity of the cage is retained. A novel coupling between the electrochemical cell and a mass spectrometer allowed the trapping of the key intermediates. Cryogenic ion spectroscopy characterization of the intermediates showed the details of the potassium ions hosting in the reduced cage and of the stabilization of the Fe-COOH intermediates by the interaction with the potassium ions at the single-molecule level.

KEYWORDS

CO₂ reduction, DFT calculations, electrochemistry, ion spectroscopy, mass spectrometry, reaction intermediates

Key points

1. Host-guest chemistry of iron porphyrin-cage catalysts in electrocatalytic CO₂ reduction results in an increase in the activity and the selectivity of the catalysis.
2. Electrochemistry–mass spectrometry coupling allowed studying of the reaction intermediates in CO₂ reduction by mass spectrometry and by helium tagging infrared photodissociation spectroscopy.

This is an open access article under the terms of the [Creative Commons Attribution](https://creativecommons.org/licenses/by/4.0/) License, which permits use, distribution and reproduction in any medium, provided the original work is properly cited.

© 2022 The Authors. *Natural Sciences* published by Wiley-VCH GmbH.

3. DFT calculations showed the details of the CO₂ reduction pathway inside of the cage cavity and the working principles of the reactivity enhancement by the host-guest chemistry.

INTRODUCTION

One of the current most pressing scientific challenges is the development of selective catalysts for the reduction of CO₂, which would enable us to process CO₂ more efficiently and at lower costs.^{1–3} Electrocatalytic CO₂ reduction seems to be the most promising direction^{4–6} and many catalysts are currently being developed.^{7–12} Optimization of their structures has led to impressively improved properties,^{13–17} but the low selectivity concerning undesired side reactions, such as hydrogen evolution, remains problematic. For a solution to this problem, one may take inspiration from enzymatic reactions, which excel in selectivity and often also in activity.^{18,19} Enzymes achieve this by binding and transforming substrates in optimized reaction pockets.²⁰ Hence, the design of synthetic catalysts should also take advantage of 3D constrained reaction sites, while keeping the electronic properties of the catalytic center(s) optimized.^{21–24}

Metalloporphyrin cages may be used to model enzymatic reactions involving heme reaction centers.²⁶ At the same time, porphyrins are among the most extensively studied catalysts for CO₂ reduction.²⁷ The systematic variation of the porphyrin backbone has converged into the currently best-performing catalyst, which is an iron tetraphenylporphyrin possessing permanently charged ammonium groups near the central metal atom (Figure 1a).^{25,28,29} Here, we go one step further and add to this design the constrained space of a diphenylglycoluril-based cage, which acts as a secondary sphere ligand to the iron center³⁰ (compound [(1)Fe^{II}], see Figure 1b). Iron porphyrin catalysts used for the

reduction of CO₂ are active in the iron(0) oxidation state, making the catalyst doubly negatively charged. Cage catalyst [(1)Fe^{II}] has a glycoluril framework with the side walls linked to the metalloporphyrin via oxyethyleneoxy spacers that can serve as crown-ether-like coordination sites for alkali metal ions. Preliminary force-field molecular dynamics simulations of aqueous systems confirm that in particular potassium ions are well positioned in the side walls (Figures S3 and S4). The DFT-calculated electrostatic potential of the iron(0) cage shows a polarized reaction pocket that might assist in the reduction of CO₂ (Figure 1c, see Supporting Information for the computational details). Hence, this suggests that the system represents a perfect case for exploring the effect of a reaction pocket on CO₂ reduction.

RESULTS AND DISCUSSION

The effect of the cage cavity on CO₂ reduction was first assessed by homogeneous electrocatalysis. The possibility to tune the electrostatic potential^{31,32} of the cage catalyst by hosting alkali metals was studied by doing experiments in electrolytes containing different cations. We compared the effect of electrolytes containing K⁺ (KBF₄ in DMF/H₂O), Na⁺ (NaBF₄ in DMF/H₂O, DMF = *N,N*-dimethylformamide), and TBA⁺ (TBABF₄ in DMF/H₂O, TBA⁺ = *n*-Bu₄N⁺). Potassium and sodium ions can coordinate with the oxyethyleneoxy units of the catalyst, whereas the TBA⁺ ions are too bulky to coordinate. Hence, in the presence

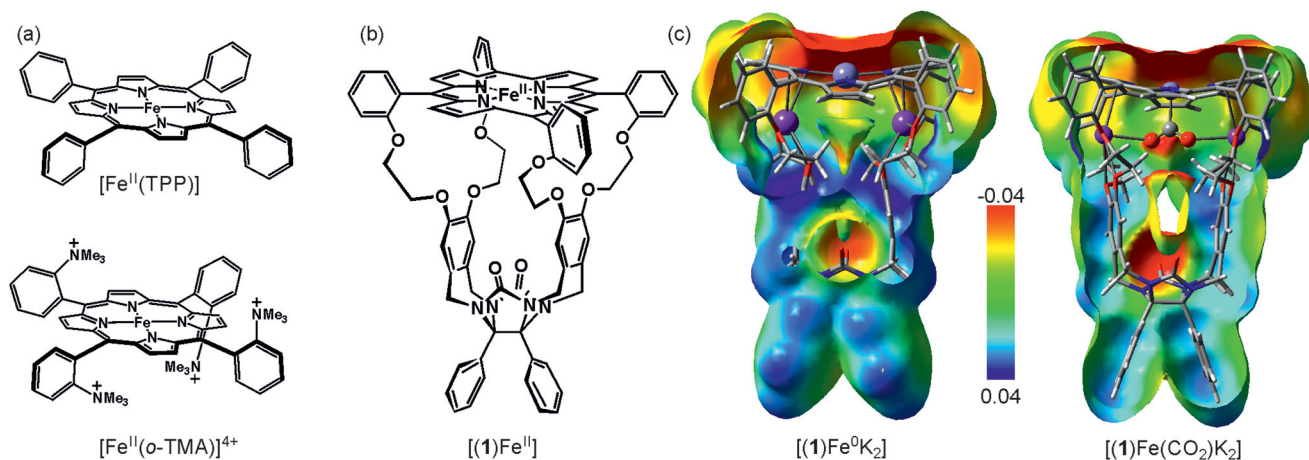


FIGURE 1 (a) Iron tetraphenylporphyrin [Fe^{II}(TPP)] and [Fe^{II}(o-TMA)]⁴⁺, which so far is the best iron porphyrin catalyst for the electrochemical reduction of CO₂.²⁵ (b) Iron cage catalyst [(1)Fe^{II}]. (c) Electrostatic potentials mapped on the electron isodensity surface (0.001) of the DFT-optimized structures of [(1)Fe⁰K₂] and [(1)Fe⁰K₂(CO₂)] (see the theoretical details). The backbone of the porphyrin cage catalyst is shown in the stick representation; the positions of the metals (Fe, K) and O-C-O are highlighted by the ball-and-stick representation. The surface is clipped from the front to show the electrostatic potential inside the cavity.

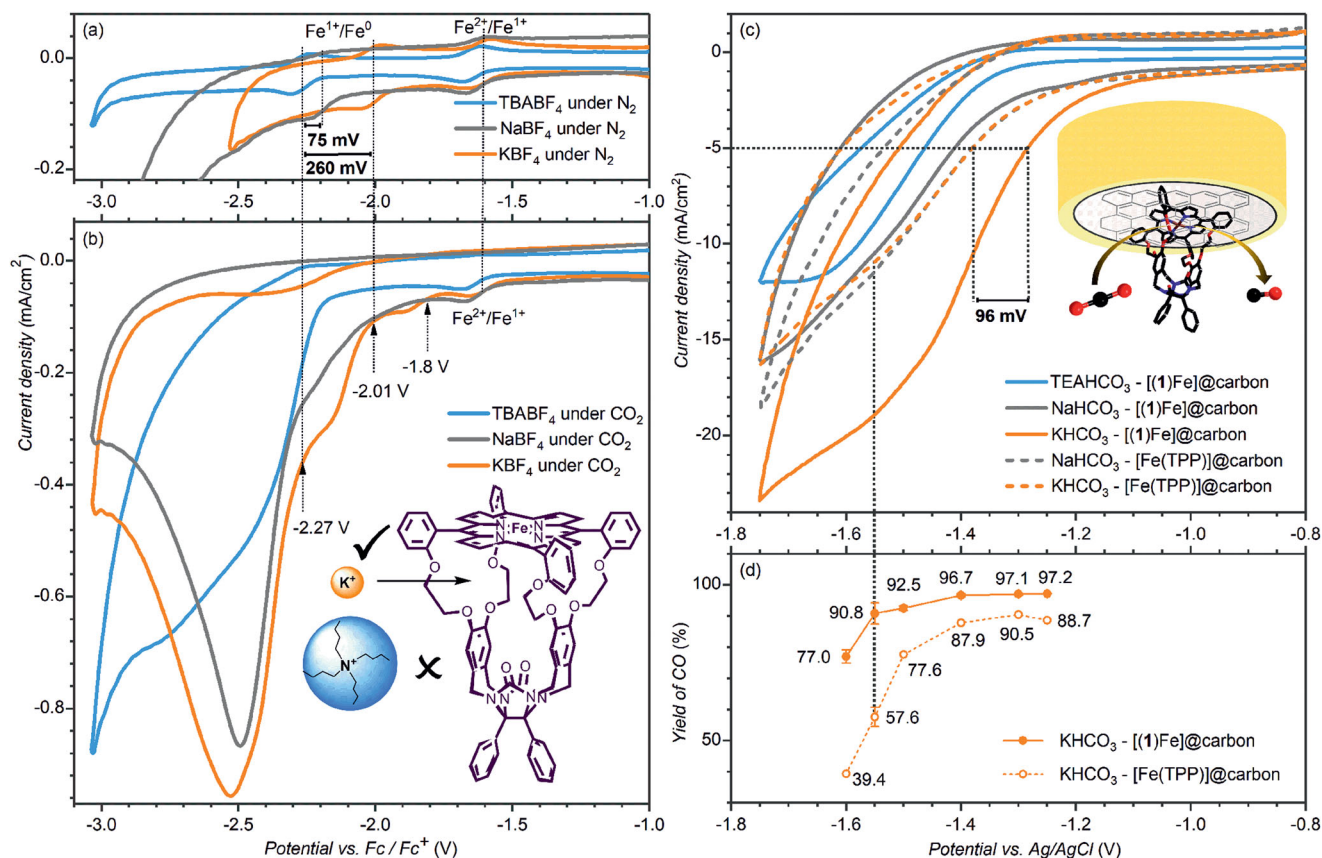


FIGURE 2 Left: Homogeneous cyclic voltammograms of [(1)Fe] (0.25 mM) measured in electrolytes containing TBABF₄ (blue), NaBF₄ (gray), and KBF₄ (orange) (0.1 M in DMF + 0.5 M H₂O; scan rate 100 mV/s) under (a) N₂ and (b) CO₂. Right: (c) Heterogeneous cyclic voltammograms of immobilized [(1)Fe]@carbon (solid lines) and [Fe(TPP)]@carbon (dashed lines) in TEAHCO₃ (blue), NaHCO₃ (gray), KHCO₃ (orange) electrolytes (0.5 M in H₂O) under CO₂ (scan rate 100 mV/s). (d) Selectivity of the CO formation in the CO₂RR catalyzed by [(1)Fe]@carbon (solid points) and [Fe(TPP)]@carbon (open points) in 0.5 M aqueous solution of KHCO₃ under CO₂

of the latter ions, we can monitor the catalytic reactivity of the cage catalyst without the charged cavity.

The cyclic voltammograms (CVs) of the [(1)Fe^{III}Cl] solutions under a nitrogen atmosphere (Figure 2a) show that the redox potential of the Fe²⁺ → Fe⁺ transition is almost unaffected by the cations of the electrolyte. Accordingly, the iron(II) cage catalyst does not coordinate with alkali metals. However, the catalytically important Fe⁺ → Fe⁰ transition is sensitive to the presence of the alkali metals (compare the blue/gray/orange curves in Figure 2a). Changing the electrolyte cations from TBA⁺ to Na⁺ or K⁺ resulted in an overpotential shift of 75 and 260 mV (E_{1/2}, Figure S5), respectively, attesting that the alkali metals coordinate to the iron(I) cage catalyst and change its electronic properties. The effect of the potassium ions is particularly strong. For comparison, the same experiments with the simple tetraphenyl porphyrin iron catalyst [Fe(TPP)] did not show any overpotential shift (Figure S5 in the Supporting Information). The electrochemistry results alone do not reveal whether the cage complexes interact with one or two potassium (sodium) ions (i.e., [(1)Fe⁰K]⁻ or [(1)Fe⁰K₂]). Later, we will show that the [(1)Fe⁰K₂] formulation is valid for the potassium complexes; therefore, we will also use it in the following for the sake of simplicity.

Under a CO₂ atmosphere, the catalytic CO₂ reduction reaction (CO₂RR) reveals itself as an increased current wave at the Fe⁺ → Fe⁰ potential (compare the blue lines in Figures 2a and 2b for CO₂RR in the TBA⁺ electrolyte). In the presence of the potassium ions, three waves beyond the Fe²⁺ → Fe⁺ reduction were detected. The first of those (−1.8 V vs. the ferrocene/ferrocenium redox couple reference, Fc/Fc⁺) occurred before the Fe⁺ → Fe⁰ reduction detected under the N₂ atmosphere (compare the orange lines in Figures 2a and 2b). This process corresponds to a one-electron reduction (Figure S6) and likely results from the binding of CO₂ to the iron(I) complex hosting the potassium ions, [(1)Fe^IK₂]⁺. The so-formed [(1)Fe^I(CO₂)K₂]⁺ complex can be reduced to iron(0) at −1.8 V.³³ Note that this feature is not observed in the TBA⁺ electrolyte, proving that the CO₂ binding to the iron(I) cage catalyst requires the interaction of K⁺ with the cage catalyst. The analysis of the reduction wave at different CV scan rates allowed us to determine the CO₂ binding rate constant to the reduced [(1)Fe⁰K₂] complex (Figure S7 and S8).^{34,35} The binding rate constant amounts to (145 ± 3) 10³ M⁻¹s⁻¹.

The next two reduction waves correspond to the catalytic CO₂RR. The first CO₂RR process appears at the Fe⁺ → Fe⁰ reduction potential observed for the cage catalyst hosting the potassium ions (at −2.01 V,

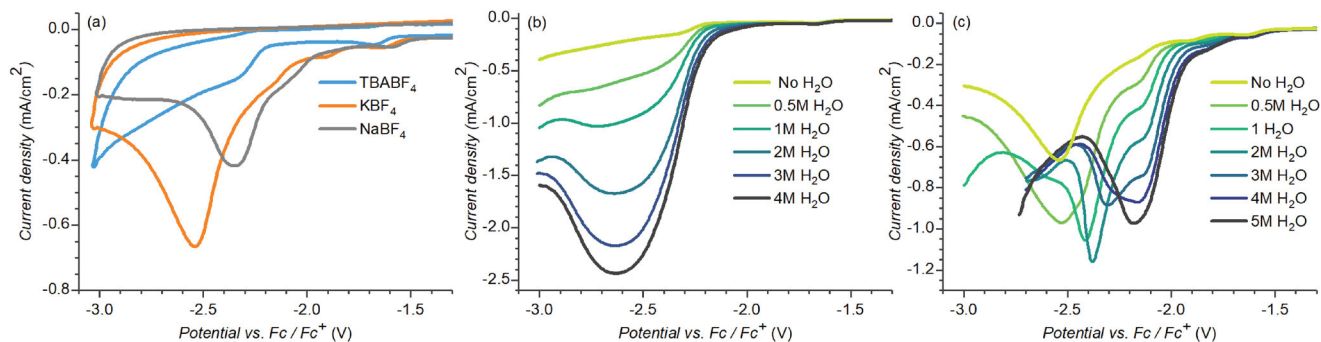


FIGURE 3 Homogeneous cyclic voltammograms of [(1)Fe] (0.25 mM) measured in a 0.1 M electrolyte (indicated in the figure) in DMF with a possible H₂O addition (indicated in the figure) saturated with CO₂ at a scan rate of 100 mV/s. (a) In dry DMF, electrolytes are color-coded. (b) Effect of H₂O addition (0–4 M) in the TBABF₄ electrolyte. (c) Effect of H₂O addition (0–5 M) in the KBF₄ electrolyte

compare the orange lines in Figures 2a and 2b). The second CO₂RR process appears at a potential of –2.27 V, which corresponds to the Fe^I → Fe⁰ reduction of the cage catalyst in the absence of the potassium ions (compare the blue line in Figure 2a and the orange line in Figure 2b). We do not observe this second Fe^I → Fe⁰ reduction under nitrogen in the presence of the K⁺ electrolyte. This implies that the CO₂RR catalyzed by [(1)Fe⁰K₂] (at –2.01 V) leads to a loss of the potassium ion(s) from the cage catalyst and generates [(1)Fe^{II}]. The bare [(1)Fe^{II}] can then be reduced sequentially to [(1)Fe^I][–] and to [(1)Fe⁰]^{2–} at the larger overpotential (–2.27 V). The availability of [(1)Fe⁰]^{2–} for the catalysis depends on the rate of the potassium ion binding to the iron(II) complex [(1)Fe^I][–], which is illustrated by the scanning rate dependence of the ratio between the processes catalyzed by [(1)Fe⁰K₂] and by [(1)Fe⁰]^{2–} (Figure S9a). The faster the scanning rate is, the shorter time is available for [(1)Fe^I][–] to complex with the potassium ions. Accordingly, the catalytic current for the CO₂RR catalyzed by bare [(1)Fe⁰]^{2–} increases. Analogous processes can also be observed in the presence of the Na⁺ electrolyte (see the gray lines in Figure 2). However, the effect of the cage-Na⁺ host-guest chemistry on the CO₂RR is weaker than that of the cage-K⁺ host-guest chemistry; therefore, we will further focus on the latter one.

The CO₂RR catalyzed by the cage catalyst with or without the K⁺ guests strongly depends on the H₂O concentration in the DMF solution (Figure 3). In the absence of H₂O, the CO₂RR most likely proceeds via the disproportionation mechanism that takes advantage of the assistance of a second CO₂ molecule to form CO and CO₃^{2–} in the catalytic electroreduction.³⁶ This mechanism is facilitated by Lewis acids such as alkali metal ions;³⁷ therefore, the CO₂RR is more efficient in the Na⁺ and K⁺ electrolytes than in the TBA⁺ electrolyte (Figure 3a). An analogous effect is also observed for the [Fe(TPP)] catalyst, albeit that the catalytic current is larger in the Na⁺ electrolyte than in the K⁺ electrolyte (Figure S10). The catalysis by the iron cage catalyst in the absence of water proceeds dominantly at the potential corresponding to the catalysis by bare [(1)Fe⁰]^{2–} without the K⁺ guests (Figure 3a). Hence, host-guest chemistry is not important for the observed CO₂RR activity under water-free conditions. Therefore, the difference between [Fe⁰(TPP)]^{2–} and [(1)Fe⁰]^{2–} is just in the cavity of the cage. A possible explanation is that alkali ions can be inside

of the cavity of the cage but not coordinate with the side walls of the cage catalyst (e.g., see Figure 5 for the structure of the mass-detected complexes [(1)Fe^{II}K]⁺). Such interactions would not change the overpotential for the reduction of the catalyst, but the alkali ions would be available to assist the CO₂RR.

Increasing the concentration of H₂O in the reaction mixture of the cage catalyst with TBA⁺ electrolyte leads to an increasing catalytic current of the CO₂RR (Figure 3b). H₂O can act as a proton source in the reduction of CO₂ to CO and H₂O. Hence, the increasing catalytic activity with the increasing H₂O concentration suggests that the mechanism changes in the presence of water because the proton-transfer reaction becomes the limiting step of the CO₂RR under these conditions. The reaction mechanism thus corresponds to the proton-assisted reduction of CO₂ leading to CO and H₂O in the presence of water in the reaction mixture.³³

In the K⁺ electrolyte, the H₂O-concentration dependence is more complex (Figure 3c). At increasing H₂O concentration, the catalytic current at the potential corresponding to the catalysis by [(1)Fe⁰K₂] (–2.01 V) also increases. The catalytic current at the potential corresponding to the catalysis by [(1)Fe⁰]^{2–} (–2.27 V) increases with a small addition of water (0.5 M). However, with a further increase of the H₂O concentration, the appearance potential of this process gradually shifts to less negative values and the catalytic current decreases. This can be interpreted by dynamic host-guest chemistry. As explained above, the CO₂RR catalyzed by [(1)Fe⁰K₂] leads to the formation of the bare [(1)Fe^{II}] complexes without the coordinated potassium ions. However, the complexes are immediately reduced during the CV experiments and the formed [(1)Fe^I][–] complexes again coordinate the potassium ions (see above). The experiments suggest that the formation of the [(1)Fe^IK₂]⁺ complexes is limited kinetically. The kinetic bottleneck is most likely associated with the kinetics of the K⁺ complexation^{38,39} with the cage catalyst, which depends on the potassium solvation shell. K⁺ interacts stronger with DMF than with H₂O (the transfer of K⁺ from H₂O to DMF is exothermic as well as exoergic).³⁸ Therefore, the transfer of K⁺ from a DMF solvation shell to the cage catalyst is likely slower than that from an H₂O solvation shell.^{38,39} Hence, an increase in the H₂O concentration should facilitate the potassium ion complexation with the cage catalyst thereby accelerating the formation of

$[(1)Fe^I K_2]^+$. Accordingly, the catalysis by $[(1)Fe^{0}]^{2-}$ is suppressed. At 5 M H_2O concentration in the solution, we observe only the CO_2RR catalyzed by $[(1)Fe^{0}K_2]$ (see the black line in Figure 3c). However, increasing the scanning rate of the CV experiment decreases the time available for the complexation with the potassium ions, and the CO_2RR catalyzed by $[(1)Fe^{0}]^{2-}$ can again be observed (Figure S9b). Finally, the peak shapes of the reduction waves suggest that the CO_2RR reaction is kinetically hindered.³⁶ The kinetic hindrance may be due to inhibition by the product, by the stabilization of an intermediate, or by the diffusion properties of the catalyst.

The diffusion limitation of the catalysis can be overcome by immobilization of the porphyrin cage catalysts onto a support.⁴⁰ At the same time, this immobilization allows the use of aqueous electrolytes, which removes a possible kinetic bottleneck of the accompanying proton-transfer reactions^{41–43} and of the potassium ion complexation rate.^{38,39} Therefore, we immobilized the cage catalyst onto an inert vulcanized conducting carbon support (see the details and Figures S11 and S12 in the Supporting Information) and performed the experiments in 0.5 M aqueous solutions of $TEAHCO_3$ ($TEA^+ = Et_4N^+$), $NaHCO_3$, and $KHCO_3$, respectively. The comparison of the cyclic voltammetry experiments in different electrolytes shows that the host-guest chemistry also works for the immobilized $[(1)Fe]$ @carbon catalyst, in analogy to the homogeneous catalysis experiments (Figure 2c, Figures S13–S16). Compared to the experiments with the electrolyte containing the non-coordinating TEA^+ , the use of Na^+ - or K^+ -based electrolytes reduced the onset potential by ~ 22 and by ~ 110 mV, respectively (Figure S15). The catalytic CO_2RR activity is not kinetically hindered and is observed only at the reduced potentials (Figure 2c).

The CO_2RR catalytic activity in water is usually larger in the presence of the alkali metal-based electrolytes than in the presence of the ammonium-based electrolytes, regardless of the identity of the catalyst.^{44,45} Therefore, we decided to assess and separate the inherent effect of the electrolytes by comparing the results obtained for the $[(1)Fe]$ @carbon catalyst with the results of the reference $[Fe(TPP)]$ @carbon catalyst under the same conditions. The onset potentials for the CO_2RR catalyzed by $[Fe(TPP)]$ @carbon were the same in all studied electrolytes (Figure S15). As expected, the catalytic activity (catalytic current) of $[Fe(TPP)]$ @carbon in alkali-metal-based electrolyte solutions was larger than that in solutions containing the $TEAHCO_3$ electrolyte (Figures S14 and S15). However, there is no significant difference between the $NaHCO_3$ and $KHCO_3$ electrolyte solutions (compare the dashed lines in Figure 2c). Hence, the significantly increased catalytic activity of the cage catalyst $[(1)Fe]$ @carbon in the presence of the $KHCO_3$ -based electrolyte as compared to the $NaHCO_3$ -based electrolyte is most likely the result of the tuning of the catalyst by host-guest interactions. The overpotential for CO_2RR catalyzed by the $[(1)Fe]$ @carbon catalyst in the $KHCO_3$ electrolyte is anodically shifted by 96 mV (at 5 mA/cm²) with respect to that of the $[Fe(TPP)]$ @carbon catalyst. Hence, the lower overpotential and the higher CO_2RR catalytic current density of $[(1)Fe]$ @carbon than those of $[Fe(TPP)]$ @carbon in the $KHCO_3$ electrolyte demonstrate the fruitful effect of the host-guest chemistry between the cage catalyst and the potassium ions on the CO_2RR catalysis.

The selectivity of catalysts is often considered to be even more important than their activity. The CO_2RR catalyzed by porphyrin-based catalysts usually yields CO along with the undesired evolution of H_2 . We compared the selectivity of the $[(1)Fe]$ @carbon catalyst for the production of CO with the selectivity of the $[Fe(TPP)]$ @carbon catalyst, by performing preparative scale electrolysis in the presence of either $TEAHCO_3$ or $KHCO_3$ as the electrolyte salts (Figure 2d and Figures S17–S20). The $CO:H_2$ selectivity of the $[(1)Fe]$ @carbon catalyst was above 90% for potentials up to -1.55 V (vs. Ag/AgCl) in both of the electrolytes, and this selectivity was always higher than that of $[Fe(TPP)]$ @carbon. Quantitative bulk experiments at -1.55 V in the presence of $KHCO_3$ -based electrolyte showed circa 90% Faradaic efficiency for CO formation with $[(1)Fe]$ @carbon and only circa 50% Faradaic efficiency with $[Fe(TPP)]$ @carbon. Hence, these results show that the cage catalyst achieves a high CO selectivity in the CO_2RR and this selectivity is also retained after boosting the activity by hosting the potassium ions.

To get a deeper insight into the host-guest chemistry of the cage catalyst and into the mechanism of the CO_2RR , we studied the intermediates in the electrochemical reaction by electrospray ionization mass spectrometry (ESI-MS).⁴⁶ Transferring the intermediates by electrospray ionization into a mass spectrometer is a challenging task,^{47–49} because these intermediates are formed at the cathode and presumably are short-lived and thus extremely low abundant in solution.⁵⁰ In addition, the reduced reactive species can be oxidized and thus be destroyed during the electrospray ionization process. Nevertheless, an optimized design of an electrochemical cell consisting of a carbon working electrode, a stainless-steel counter electrode, and a Pt wire pseudoreference electrode controlled by a floating potentiostat assembly (Figure S21) enabled us to detect the desired reduced species (Figure 4). The electrochemically formed complexes are transferred by a silica capillary that is sandwiched in between two carbon sheets of the working electrode directly connected to the electrospray ionization source of a mass spectrometer.

The ESI-MS experiments were performed with acetonitrile solutions. This solvent is more suitable for the ESI-MS experiments than DMF. The iron cage catalyst shows analogous electrochemical CO_2RR properties in acetonitrile as in DMF (Figure S22). The reference ESI-MS spectrum of an acetonitrile solution of $[(1)Fe^{III}(Cl)]$ and KBF_4 showed one dominant signal for $[(1)Fe^{III}(Cl)K]^+$ (Figure 4a). After applying a negative voltage (-3 V), the signal of $[(1)Fe^{III}(Cl)K]^+$ depleted and the spectra showed the formation of Fe^{II} complexes in the positive mode and Fe^I complexes in the negative mode (Figure 4 and Figure S23, respectively). The reactive Fe^0 complexes should be either neutral $[(1)Fe^0K_2]$ or anionic $[(1)Fe^0K]^-$ and $[(1)Fe^0]^{2-}$ species. The neutral complexes cannot be detected by mass spectrometry and the reactive $[(1)Fe^0]^{2-}$ anions likely easily lose an electron during the ionization process⁵¹ to form the detected $[(1)Fe^I]^-$. Therefore, their absence in the spectra is not surprising. After saturation of the solution with CO_2 , new complexes appeared (see color-highlighted signals in Figures 4b and 4c). The detected intermediates contain the CO_2H group and correspond to positively charged $[(1)Fe^{II}(CO_2H)K_2]^+$ and negatively charged $[(1)Fe^{II}(CO_2H)]^-$. These intermediates are formed by the

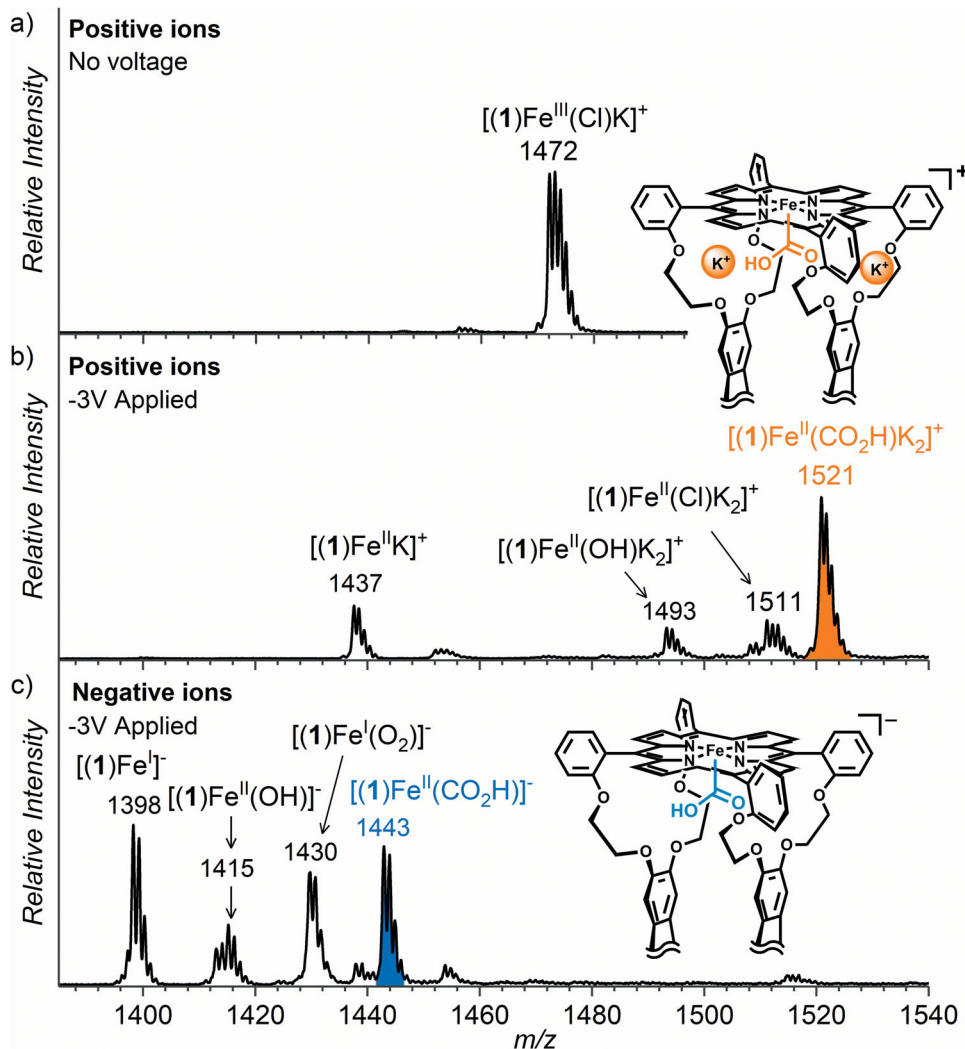


FIGURE 4 (a) EC-ESI-MS (electrochemistry–electrospray ionization mass spectrometry) spectra of an acetonitrile solution of [(1)Fe^{III}Cl] (0.143 mM) and KBF₄ (0.150 mM) measured under the N₂ atmosphere without applying a voltage. (b,c) The same experiment but now under a CO₂ atmosphere at –40°C with an applied voltage of –3 V (vs. Pt wire reference electrode) in the positive (b) and the negative (c) ion mode

reaction of either [(1)Fe⁰K₂] or [(1)Fe⁰]²⁻, respectively, with CO₂, followed by protonation. Both complexes probably have a short lifetime and therefore can only be trapped at a low temperature (–40°C). This is the first time that such intermediates in CO₂RR have been detected by mass spectrometry, which opens the possibility to study their unimolecular properties and their spectroscopic characteristics.

The collision-induced dissociation (CID) of the intermediates leads almost exclusively to the elimination of CO and the formation of the corresponding iron-hydroxo complexes [(1)Fe^{II}(OH)K₂]⁺ and [(1)Fe^{II}(OH)]⁻ (Figure S25). These product complexes are also detected in the mass spectra taken directly from the solution and they are formed only in the presence of CO₂ (cf. Figure 4 and Figures S23 and S24). The energy required for the elimination of CO from the Fe-COOH intermediates can be determined by energy-resolved CID experiments.^{52,53} The bond dissociation energy (BDE) for the CO loss from [(1)Fe^{II}(CO₂H)K₂]⁺ amounts to 1.29 ± 0.05 eV and that from [(1)Fe^{II}(CO₂H)]⁻ to 1.24 ± 0.10 eV (Figure S28). Hence, the hosting of the potassium ions in the cage does not significantly affect the

energy demand of the rate-determining C–O bond cleavage (at least in the gas phase).^{54,55} In solution, alternative pathways of the C–O bond cleavage exist, namely, the Fe-COOH intermediates can eliminate H₂O after an additional protonation. This reaction pathway leads to the iron(II) carbonyl complexes.^{35,56} We did not detect these complexes under any experimental conditions.⁵⁶ Presumably, the complexes are rapidly reduced to iron(I) carbonyl complexes and then eliminate the CO molecule.

The structure of the isolated [(1)Fe^{II}(CO₂H)K₂]⁺ intermediate was characterized by cryogenic infrared photodissociation (IRPD) spectroscopy (Figure 5).^{57–62} The interpretation of the spectrum of [(1)Fe^{II}(CO₂H)K₂]⁺ is based on a comparison with the IRPD spectra of the related [(1)Fe^{II}K]⁺ and [(1)Fe^{II}(Cl)K₂]⁺ complexes. The IRPD spectra of these reference ions differ in the position of the C–O stretching and CH₂ deformation vibrations of the oxyethyleneoxy side walls of the cage ligand and in the position of the urea carbonyl vibrations (see highlighted areas in Figure 5a). The urea carbonyl vibrations of [(1)Fe^{II}K]⁺ are slightly red-shifted compared to those of

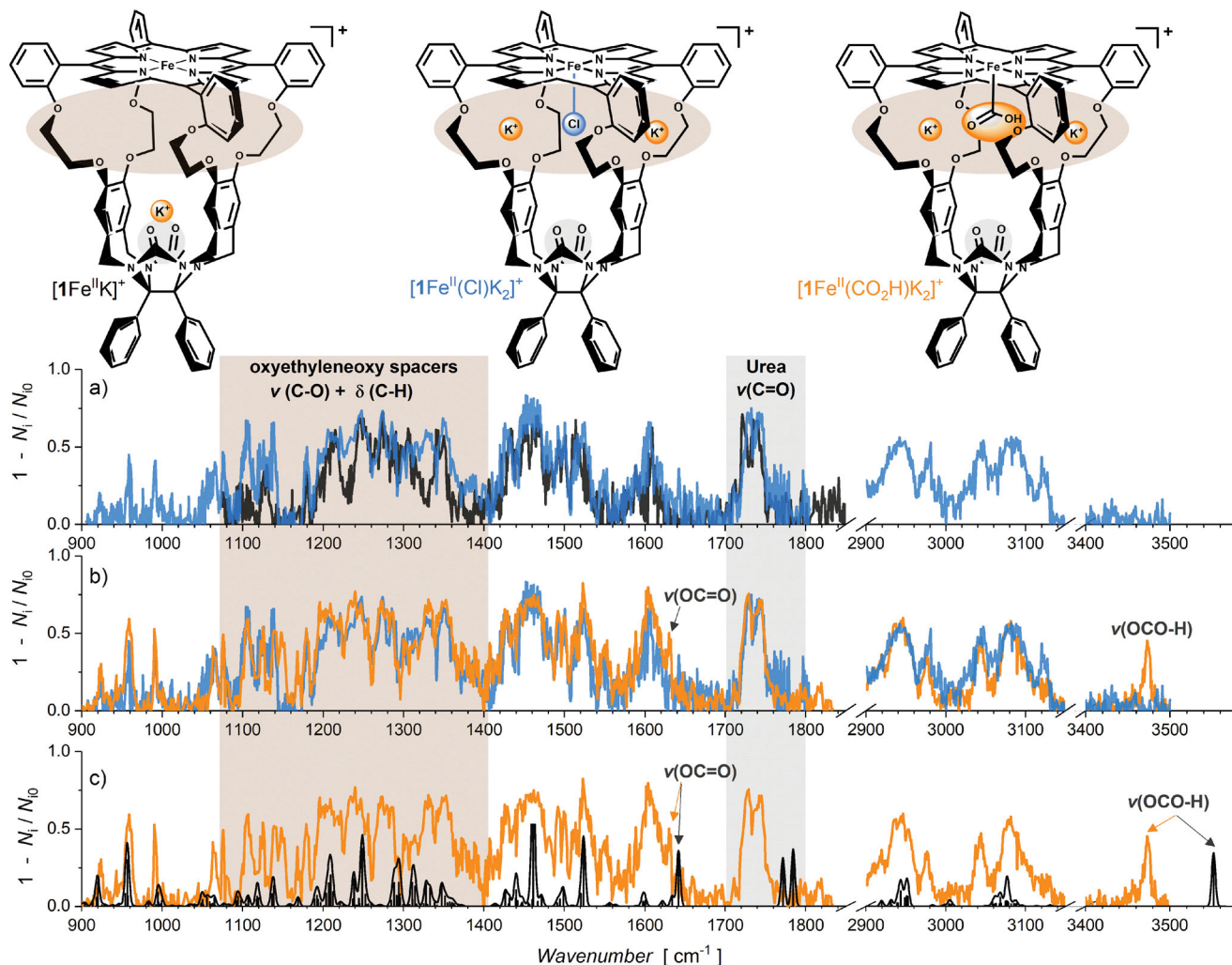


FIGURE 5 (a) IRPD spectra of the mass-selected ions $[(1)\text{Fe}^{\text{II}}(\text{Cl})\text{K}_2]^+$ (blue) and $[(1)\text{Fe}^{\text{II}}\text{K}]^+$ (black). (b) IRPD spectra of the mass-selected ions $[(1)\text{Fe}^{\text{II}}(\text{Cl})\text{K}_2]^+$ (blue) and $[(1)\text{Fe}^{\text{II}}(\text{CO}_2\text{H})\text{K}_2]^+$ (orange). (c) Theoretical IR spectrum of gaseous $[(1)\text{Fe}^{\text{II}}(\text{CO}_2\text{H})\text{K}_2]^+$ (black, B3LYP-D3/def2SVP; see also Figure S30) and the IRPD spectrum of $[(1)\text{Fe}^{\text{II}}(\text{CO}_2\text{H})\text{K}_2]^+$ (orange)

$[(1)\text{Fe}^{\text{II}}(\text{Cl})\text{K}_2]^+$, suggesting that the potassium ion in the $[(1)\text{Fe}^{\text{II}}\text{K}]^+$ complex is coordinated in the vicinity of the carbonyl groups (see also a comparison with the spectrum of $[(1)\text{Fe}^{\text{III}}]^+$ in Figure S29). The differences in the crown ether-like moiety range suggest that the two potassium ions of $[(1)\text{Fe}^{\text{II}}(\text{Cl})\text{K}_2]^+$ are likely coordinated to the oxyethyleneoxy functions attached to the side walls of the cage compound.

The IRPD spectrum of the $[(1)\text{Fe}^{\text{II}}(\text{CO}_2\text{H})\text{K}_2]^+$ intermediate is almost identical to that of $[(1)\text{Fe}^{\text{II}}(\text{Cl})\text{K}_2]^+$ attesting the same mode of K^+ coordination, that is, to the oxyethyleneoxy functions of the cage. The presence of the hydroxycarbonyl functionality is evidenced by the additional peaks in the IRPD spectrum of $[(1)\text{Fe}^{\text{II}}(\text{CO}_2\text{H})\text{K}_2]^+$ in comparison to that of $[(1)\text{Fe}^{\text{II}}(\text{Cl})\text{K}_2]^+$: the O-H vibration is at 3473 cm^{-1} and the C = O vibration at 1630 cm^{-1} . For comparison, the C = O vibration of the independently generated formate (O-coordinated carboxylate) complex $[(1)\text{Fe}^{\text{II}}(\text{OCO})\text{K}_2]^+$ is at 1638 cm^{-1} (Figure S29) and the CO frequency of a recently detected iron porphyrinoid hydroxycarbonyl in solution is 1682 cm^{-1} .^{53,63} Our assignment was further

corroborated by DFT calculations. The hydroxycarbonyl group of the most stable isomer of $[(1)\text{Fe}^{\text{II}}(\text{CO}_2\text{H})\text{K}_2]^+$ is coordinated inside of the iron cage and it is stabilized by the interactions between the oxygen atoms of the hydroxycarbonyl group and the potassium ions coordinated at the side-wall oxyethyleneoxy units (see Figures S30 and S31 for the DFT calculations in the gas phase). The theoretical IR spectrum reproduces all features in the experimental IRPD spectrum and confirms the structure of the intermediate (Figure 5c). Alternative structures with different coordination sides of the potassium ions are less energetically favored and their IR spectra do not agree with the experimental one (Figure S30).

Finally, we explored the mechanism of the CO_2RR by DFT calculations (Figure 6). The calculations suggest that $[(1)\text{Fe}^{\text{II}}]^+$ has a quintet ground state.^{64,65} The complexation of CO_2 at the inside of the cavity is associated with a spin change to the triplet state and is slightly endoergic. The C-binding of CO_2 to the iron center is associated with a two-electron transfer from iron to CO_2 and leads to the singlet state $^1[(1)\text{Fe}(\text{CO}_2)]^{2-}$ complex that is protonated in a strongly exoergic

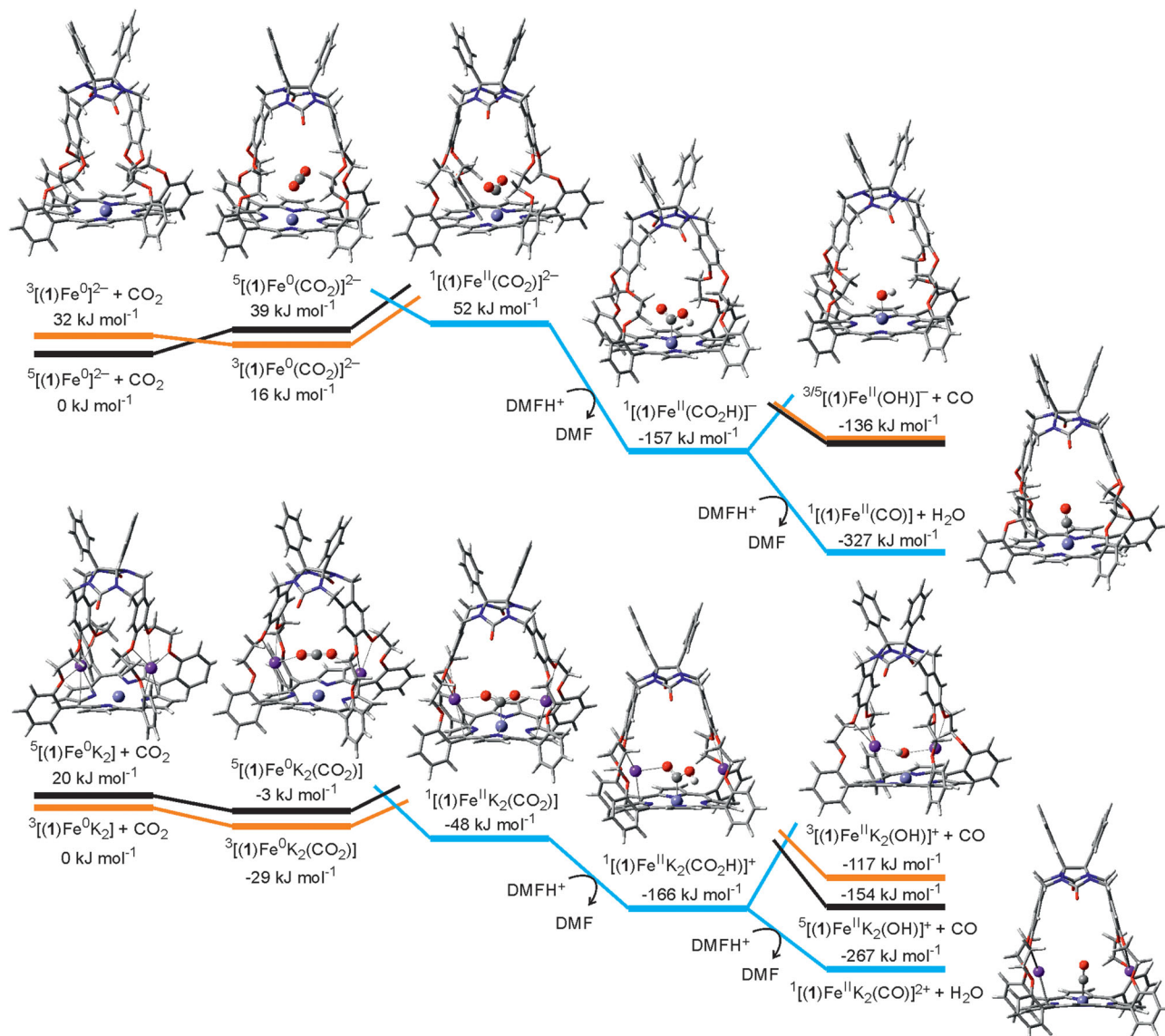


FIGURE 6 Relative Gibbs free energies of minima on potential energy surfaces (M06L-D3/def2SVP, SMD solvation model for DMF) for the reaction of $[(1)Fe^0]^{2-}$ (top) and $[(1)Fe^0K_2]$ (bottom) with CO₂, respectively. The energies are at 298 K and 1 atm in the DMF solvation model. Relative energies at 0 K can be found in the Supporting Information (Figure S32). The positions of Fe, K, and CO₂ are highlighted by using a ball and stick presentation. The depicted structures correspond to the given ground states. The energy levels are spin-state color-coded: blue = singlet, orange = triplet, black = quintet.

step to form the detected intermediate $[(1)Fe(CO_2H)]^-$. Here, we have approximated the protonation as a reaction with a protonated DMF molecule (other approaches confirm the exoergic nature of this step, albeit with slightly different values). From here, the CO elimination leads to $[(1)Fe(OH)]^-$. This step is slightly endoergic and it is associated with a spin flip (the calculations predict the same energy for the triplet and the quintet state). An alternative path proceeds via protonation and subsequent H₂O elimination. We have again assumed protonation by DMFH⁺ leading to neutral $[(1)Fe^{II}(CO)]$, H₂O, and DMF. Note that the calculated energetics of this step will strongly depend on the solvation model as it corresponds to the reaction between a cation and an anion leading to neutral molecules. At our level of theory, this step is strongly exoergic.

Introducing potassium cations in the cage stabilizes the triplet state as the ground state of the starting complex $[(1)Fe^0K_2]$. The complex binds CO₂ inside the cavity with both oxygen atoms weakly coordinated to the potassium ions and the process is exoergic. The electrostatic field of the potassium ions in $^3[(1)FeK_2(CO_2)]$ makes the following two-electron reduction step toward the singlet state complex $^1[(1)FeK_2(CO_2)]$ exoergic because the potassium ions stabilize the negative charge formed at the oxygen atoms (as also suggested in Figure 1). The subsequent protonation of the $^1[(1)FeK_2(CO_2)]$ intermediate to form $^1[(1)FeK_2(CO_2H)]^+$ is strongly exoergic. The final step of CO elimination is associated with a spin flip to the quintet state and is endoergic. The alternative final sequence of the protonation and the subsequent H₂O elimination is again challenging to estimate

computationally at our level of theory. We have assumed protonation of $^1[(1)\text{FeK}_2(\text{CO}_2\text{H})]^+$ by DMFH^+ leading to $^1[(1)\text{FeK}_2(\text{CO})]^{2+}$, H_2O , and DMF. This sequence is exoergic giving the overall energy balance of -267 kJ mol^{-1} . Finally, the experiments suggest that the cage catalyst loses the potassium ion(s) after the CO_2RR . Presumably, the last step of the C-O bond cleavage in the $^1[(1)\text{FeK}_2(\text{CO}_2\text{H})]^+$ cation could be K^+ -assisted toward the formation of $^1[(1)\text{FeK}_2(\text{CO})]^{2+}$ and KOH .⁶⁶ Such a step, however, is strongly endoergic at our level of theory ($\Delta\Delta G^{298\text{K}} > 200 \text{ kJ mol}^{-1}$).

In general, the comparison of both potential energy surfaces shows that the placing of the positively charged ions above the porphyrin plane inverts the key steps of the CO_2 reduction (coordination and two-electron reduction) from being endoergic to being exoergic. Hence, it rationalizes a large activity of the cage catalyst $[(1)\text{Fe}^0\text{K}_2]$ as well as of the previously published $[\text{Fe}^{\text{II}}(\text{o-TMA})]^{4+}$.²⁵ We expect this to be a qualitatively solid observation independent of the DFT model. The subsequent protonation steps are all exoergic. However, the calculated values strongly depend on the solvation model and should be taken only as an estimate of the trend. More accurate calculations should, in principle, employ an explicit solvation model. However, these calculations are extremely demanding and beyond the scope of the present paper. We will address this in a future publication (see preliminary results in the Supporting Information).

CONCLUSIONS

The iron porphyrin glycoluril-based cage complex $[(1)\text{Fe}]$ offers a constrained reaction site that promotes the electrochemical reduction of CO_2 to CO with a selectivity that is largely superior to that of the reference iron tetraphenylporphyrin complex. In addition, we show that the host-guest chemistry of the cage can be used to modify simultaneously the electronic properties of the metal center and the secondary coordination sphere in favor of the catalysis. The oxyethyleneoxy functions attached to the side walls of the cage catalyst are optimal for hosting the potassium ions, which opens the possibility to use the electrolyte containing this ion for tuning the electronic properties of the catalyst. The immobilized iron cage catalyst $[(1)\text{Fe}]@\text{carbon}$ hosting K^+ ions (from the electrolyte) shows both a lower overpotential (by 96 mV at 5 mA/cm^2) and a higher catalytic activity for CO_2RR than the reference immobilized iron tetraphenyl porphyrin catalyst $[(\text{Fe}(\text{TPP}))@\text{carbon}]$. The host-guest tuning of the catalyst properties does not deteriorate the superior selectivity offered by the cage cavity, altogether making $[(1)\text{Fe}]@\text{carbon}$ an excellent catalyst for electrochemical CO_2RR in the KHCO_3 -based electrolyte. The combination of electrochemistry and electrospray ionization mass spectrometry allowed us to detect the key intermediates of the reaction, that is, $[(1)\text{Fe}^{\text{II}}(\text{CO}_2\text{H})\text{K}_2]^+$ and $[(1)\text{Fe}^{\text{II}}(\text{CO}_2\text{H})]^-$. The structure of the $[(1)\text{Fe}^{\text{II}}(\text{CO}_2\text{H})\text{K}_2]^+$ intermediate including the details of the potassium binding was unraveled by cryogenic ion spectroscopy of the isolated ions. DFT calculations showed that the favorable electrostatic potential formed by the potassium ions makes all steps of CO_2RR exoergic. Especially, the key step of two-electron reduction to form the $\text{Fe}^{\text{II}}\text{-COO}^-$ intermedi-

ate is endothermic for $[(1)\text{Fe}(\text{CO}_2)]^{2-}$, but becomes exothermic for $[(1)\text{Fe}^{\text{II}}(\text{CO}_2)\text{K}_2]$.

EXPERIMENTAL AND COMPUTATIONAL DETAILS

Materials

Chemicals were obtained from commercial sources. The diphenylglycoluril-based cage ligand 1H_2 was prepared according to the published procedure.⁶⁷ The iron complex $[(1)\text{Fe}^{\text{III}}\text{Cl}]$ was prepared using a common procedure with $[\text{FeCl}_2(\text{H}_2\text{O})_4]$ and characterized (UV-vis (CHCl_3) λ_{max} , nm (ϵ): 416 ($3.07 \times 10^5 \text{ L}\cdot\text{mol}^{-1}\cdot\text{cm}^{-1}$), 510 ($3.81 \times 10^4 \text{ L}\cdot\text{mol}^{-1}\cdot\text{cm}^{-1}$), 574 ($1.30 \times 10^4 \text{ L}\cdot\text{mol}^{-1}\cdot\text{cm}^{-1}$). Emission (CHCl_3 , $\lambda_{\text{excitation}} = 416 \text{ nm}$) λ_{max} , nm: 472, 650, 717. HRMS: calcd. for $[\text{C}_{84}\text{H}_{62}\text{N}_8\text{O}_{10}\text{Fe}\cdot\text{CH}_3\text{OH}]^+$ 1430.42037, found 1430.39428.). For more details, see the Supporting Information.

Electrochemistry

Homogeneous cyclic voltammetry experiments were performed using a standard three-electrode assembly in a solution of 0.25 mM catalyst, 0.1 M of a supporting electrolyte (TBABF_4 , NaBF_4 , and KBF_4), and 0 M $-5 \text{ M H}_2\text{O}$ in DMF (10 mL). We used a glassy carbon working electrode, a double junction nonaqueous Ag/AgCl reference electrode filled with 2 M LiCl in ethanol as the inner electrolyte, and a platinum mesh of 2 cm^2 area as the counterelectrode. The reference electrode was calibrated against the ferrocene/ferrocenium redox couple. Before the measurements, the solution was bubbled with N_2 or CO_2 for 30 min and during the measurements, the corresponding gas was kept flowing through the head space.

Heterogeneous CV experiments were performed with the catalyst deposited at vulcanized carbon black (the optimized mass ratio of carbon to the catalyst was 1:1/6, see the Supporting Information for the details of the preparation and the optimization (Section 4.2)). The catalyst ink ($10 \mu\text{L}$) was drop-casted on a clean glassy carbon electrode and air-dried (using an infrared light lamp). The reference electrode was an aqueous Ag/AgCl reference electrode filled with 3 M KCl . The CVs were recorded in an aqueous bicarbonate solution (0.5 M) of different electrolytes (TEAHCO_3 , NaHCO_3 , KHCO_3) purged either with N_2 or with CO_2 for 30 min. A blank experiment performed only with carbon black in KHCO_3 did not show any CO_2RR activity (Figure S13). Product analysis was done by performing preparative controlled potential electrolysis (CPE) at different polarization voltages. We used a modified H-cell (Figure S17) with three compartments, a working electrode and a counterelectrode separated by a Nafion proton exchange membrane (activated before the assembly), and an additional CO_2 saturation compartment. The saturation compartment was attached to the working electrode through an opening, allowing a free mixing of electrolytes between compartments. The headspace of the working electrode was held airtight and connected to an in-line gas chromatograph. The catalyst ink ($500 \mu\text{L}$) was drop-cast ($10 \mu\text{L} \times 50$) on a Toray carbon paper

electrode (area = 1 cm²) and dried in the air (using IR Lamp). The reference electrode (aq. Ag/AgCl-3 M KCl) was placed close to the working electrode. A platinum wire gauze (geometrical area approximately 11 cm²) was used as the counterelectrode. The headspace of the cathode compartment was calibrated by injecting known volumes of CO and H₂. Before the measurement, the electrolyte was deoxygenated with N₂ purging and then saturated with CO₂. The CO₂ bubbling was continued in the saturation compartment and the electrolyte was stirred during the measurement (10 min). The gaseous products from the cathode head space were analyzed by the in-line GC (see more details in the Supporting Information). Extended electrolysis for 2 h at -1.4 V (vs. Ag/AgCl) and subsequent NMR (nuclear magnetic resonance) analysis was performed to check the possible formation of liquid products.

Mass spectrometry

Electrospray ionization mass spectrometry (ESI-MS) spectra were measured with a Paul-type ion trap mass spectrometer (LCQ from Thermo) connected through a silica capillary to a gas-tight, small-volume single-compartment electrochemical cell with three electrode assembly (a stainless-steel counterelectrode, a Pt wire reference electrode–pseudoreference electrode, and a Toray carbon working electrode). The silica capillary was sandwiched in between two Toray carbon sheets of the working electrode. The electrochemically generated species on the surface of the working electrode were transferred with the capillary (using N₂/CO₂ overpressure in the cell) to the mass spectrometer. The polarization of the electrode was controlled using a USB-powered potentiostat (Ivium pocketSTAT2, USB = universal serial bus). The interference from the high voltage of the ESI source was eliminated by operating a potentiostat without a ground connection (floating). A 5 kV USB isolator was used between the connection to the computer to decouple the potentiostat from the ground contact (see the Supporting Information for further details). The solutions consisted of the cage catalyst (0.8 mg) dissolved in 0.5 mL of DCM and diluted to 4 mL with acetonitrile (ACN) to a final concentration of 143 μM with the addition of the KBF₄ salt (150 μM) serving as both supporting electrolyte and K⁺ ion source (see more details and results in the Supporting Information (Section 5), Figure S21).

Ion spectroscopy

The helium tagging IRPD spectra were measured with the ISORI instrument.^{58,68} The ions were generated in the same way as for the electrochemistry mass spectrometry study. The ions of interest were mass-selected by a quadrupole mass filter and guided to a cold ion trap (~10 K) by an octopole ion guide. The ions were trapped and thermalized in collisions with helium buffer gas. The cold ions formed complexes with helium MHe⁺ that were used for monitoring IR photon absorption. The trapped ions were irradiated by a tunable NdYAG laser-pumped OPO/OPA system (optical parametric oscillator/optical parametric amplifier from Laser Vision). After the irradiation, the ions were extracted from the trap, mass-analyzed by a quadrupole, and

detected with a Daly-type detector working in the counting mode. The absorption of given photons (ν_i) was monitored as a depletion of the number of the MHe⁺ complexes (N_0). The spectrum is plotted as $1 - N(\nu_i)/N_0$, where $N(\nu_i)$ and N_0 were measured in alternating cycles with or without the laser beam admitted to the trap (for more details, see the Supporting Information).

DFT calculations

The preliminary calculations (Figure 1) were performed in the gas phase using the M06L functional⁶⁹ with the D3 dispersion⁷⁰ correction and with the def2SVP basis set⁷¹ as implemented in the Gaussian program. The exploration of the mechanism (Figure 6) was performed at the same level but included the SMD solvation model for DMF. The relative Gibbs energies were corrected for the change in the number of the moles (n) in a reaction step by a correction of $(7.9 \Delta n) \text{ kJ mol}^{-1}$. The relative energies at 0 K are shown in Figure S32. The IRPD spectra are compared to the harmonic theoretical IR spectra calculated in the gas phase at the B3LYP-D3/def2SVP of theory.^{72–74} The scaling factor is 0.978. All reported results are for the minima on the potential energy surfaces as verified by the Hessian calculations.

AUTHORS CONTRIBUTION

Adarsh Koovakattil Surendran: data curation; formal analysis, investigation, methodology, visualization, writing—original draft, writing—review & editing. Guilherme L. Tripodi: data curation, formal analysis, investigation, visualization. Eva Pluhařová: investigation, writing—review & editing. Aleksandr Y. Pereverzev: methodology. Jeroen P. J. Bruekers: investigation. Johannes A. A. W. Elemans: supervision, writing—review & editing. Evert Jan Meijer: supervision, funding acquisition, writing—review & editing. Jana Roithová: conceptualization, funding acquisition, investigation, methodology, project administration, supervision, visualization, writing—review & editing.

ACKNOWLEDGMENT

The work was supported by the Netherlands Organization for Scientific Research (NWO, 740.018.022 and VI.C.192.044) and through the HRSMC fellowship to E.P.

CONFLICT OF INTEREST

Jana Roithová is a coauthor of the manuscript and a member of the Advisory Board of Natural Sciences and was not involved in the handling of the peer-review process of this submission.

DATA AVAILABILITY STATEMENT

Data will be available at the Radboud University repository.

ETHICS STATEMENT

The authors confirm that they have followed the ethical policies of the journal.

ORCID

Jana Roithová  <https://orcid.org/0000-0001-5144-0688>

PEER REVIEW

The peer review history for this article is available at <https://publons.com/publon/10.1002/ntls.20220019>

REFERENCES

- Ampelli C, Perathoner S, Centi G. CO₂ utilization: an enabling element to move to a resource- and energy-efficient chemical and fuel production. *Philos Trans R Soc A Math Phys Eng Sci.* 2015;373:20140177.
- Chen C, Khosrowabadi Kotyk JF, Sheehan SW. Progress toward commercial application of electrochemical carbon dioxide reduction. *Chem.* 2018;4:2571-2586.
- Francke R, Schille B, Roemelt M. Homogeneously catalyzed electroreduction of carbon dioxide-methods, mechanisms, and catalysts. *Chem Rev.* 2018;118:4631-4701.
- Garg S, Li M, Weber AZ, et al. Advances and challenges in electrochemical CO₂ reduction processes: an engineering and design perspective looking beyond new catalyst materials. *J Mater Chem A.* 2020;8:1511-1544.
- Jin S, Hao Z, Zhang K, Yan Z, Chen J. Advances and challenges for the electrochemical reduction of CO₂ to CO: from fundamentals to industrialization. *Angew Chem Int Ed.* 2021;60:20627-20648.
- Birdja YY, Pérez-Gallent E, Figueiredo MC, Göttle AJ, Calle-Vallejo F, Koper MTM. Advances and challenges in understanding the electrocatalytic conversion of carbon dioxide to fuels. *Nat Energy.* 2019;4:732-745.
- Johnson D, Qiao Z, Djire A. Progress and challenges of carbon dioxide reduction reaction on transition metal based electrocatalysts. *ACS Appl. Energy Mater.* 2021;4:8661-8684.
- Corbin N, Zeng J, Williams K, Manthiram K. Heterogeneous molecular catalysts for electrocatalytic CO₂ reduction. *Nano Res.* 2019;12:2093-2125.
- Liu A, Gao M, Ren X, et al. Current progress in electrocatalytic carbon dioxide reduction to fuels on heterogeneous catalysts. *J Mater Chem A.* 2020;8:3541-3562.
- Kornienko N, Zhao Y, Kley CS, et al. Metal-organic frameworks for electrocatalytic reduction of carbon dioxide. *J Am Chem Soc.* 2015;137:14129-14135.
- Li X, Wang S, Li L, Sun Y, Xie Y. *J Am Chem Soc.* 2020;142:9567-9581.
- Zhu Q, Murphy CJ, Baker LR. Opportunities for electrocatalytic CO₂ reduction enabled by surface ligands. *J Am Chem Soc.* 2022;144:2829-2840.
- Elouarzaki K, Kannan V, Jose V, Sabharwal HS, Lee J-M. Recent trends, benchmarking, and challenges of electrochemical reduction of CO₂ by molecular catalysts. *Adv Energy Mater.* 2019;9:1900090.
- Boutin E, Merakeb L, Ma B, et al. Molecular catalysis of CO₂ reduction: recent advances and perspectives in electrochemical and light-driven processes with selected Fe, Ni and Co aza macrocyclic and polypyridine complexes. *Chem Soc Rev.* 2020;49:5772-5809.
- Costentin C, Robert M, Savéant J-M, Tatin A. Efficient and selective molecular catalyst for the CO₂ -to-CO electrochemical conversion in water. *Proc Natl Acad Sci USA.* 2015;112:6882-6886.
- Robert M, Costentin C, Daasbjerg K. *Carbon Dioxide Electrochemistry: Homogeneous and Heterogeneous Catalysts.* The Royal Society Of Chemistry; 2020.
- Wang J, Dou S, Wang X. Structural tuning of heterogeneous molecular catalysts for electrochemical energy conversion. *Sci Adv.* 2021;7:eabf3989.
- Jayathilake BS, Bhattacharya S, Vaidehi N, Narayanan SR. Efficient and selective electrochemically driven enzyme-catalyzed reduction of carbon dioxide to formate using formate dehydrogenase and an artificial cofactor. *Acc Chem Res.* 2019;52:676-685.
- Contaldo U, Guigliarelli B, Perard J, Rinaldi C, Le Goff A, Cavazza C. Efficient electrochemical CO₂ /CO interconversion by an engineered carbon monoxide dehydrogenase on a gas-diffusion carbon nanotube-based bioelectrode. *ACS Catal.* 2021;11:5808-5817.
- Stoffel GMM, Saez DA, Demirci H, et al. Four amino acids define the CO₂ binding pocket of enoyl-CoA carboxylases/reductases. *Proc Natl Acad Sci USA.* 2019;116:13964-13969.
- Smith PT, Benke BP, Cao Z, et al. Iron porphyrins embedded into a supramolecular porous organic cage for electrochemical CO₂ reduction in water. *Angew Chem Int Ed.* 2018;57:9684-9688.
- Chen Y, Li P, Noh H, et al. Stabilization of formate dehydrogenase in a metal-organic framework for bioelectrocatalytic reduction of CO₂. *Angew Chem Int Ed.* 2019;58:7682-7686.
- Liu D-C, Wang H-J, Wang J-W, Zhong Di-C, Jiang L, Lu T-Bu. Highly efficient and selective visible-light driven CO₂ -to-CO conversion by a Co-based cryptate in H₂ O/CH₃ CN solution. *Chem Commun.* 2018;54:11308-11311.
- Margarit CG, Schnedermann C, Asimow NG, Nocera DG. Carbon dioxide reduction by iron hangman porphyrins. *Organometallics.* 2019;38:1219-1223.
- Azcarate I, Costentin C, Robert M, Savéant J-M. Through-space charge interaction substituent effects in molecular catalysis leading to the design of the most efficient catalyst of CO₂ -to-CO electrochemical conversion. *J Am Chem Soc.* 2016;138:16639-16644.
- Hessenauer-Ilicheva N, Franke A, Meyer D, Woggon W-D, Van Eldik R. Mechanistic insight into formation of oxo-iron(IV) porphyrin-cation radicals from enzyme mimics of cytochrome P450 in organic solvents. *Chem - A Eur J.* 2009;15:2941-2959.
- Gotico P, Halime Z, Aukauloo A. Recent advances in metalloporphyrin-based catalyst design towards carbon dioxide reduction: from bio-inspired second coordination sphere modifications to hierarchical architectures. *Dalton Trans.* 2020;49:2381-2396.
- Martin DJ, Mayer JM. Oriented electrostatic effects on O₂ and CO₂ reduction by a polycationic iron porphyrin. *J Am Chem Soc.* 2021;143:11423-11434.
- Hong D, Kawanishi T, Tsukakoshi Y, Kotani H, Ishizuka T, Kojima T. Efficient photocatalytic CO₂ reduction by a Ni(II) complex having pyridine pendants through capturing a Mg²⁺ ion as a Lewis-acid cocatalyst. *J Am Chem Soc.* 2019;141:20309-20317.
- Elemans JAAW, Nolte RJM. Porphyrin cage compounds based on glycoluril - from enzyme mimics to functional molecular machines. *Chem Commun.* 2019;55:9590-9605.
- Shaik S, Stuyver T. *Effects of Electric Fields on Structure and Reactivity: New Horizons in Chemistry.* The Royal Society Of Chemistry; 2021.
- Shaik S, Danovich D, Joy J, Wang Z, Stuyver T. Electric-field mediated chemistry: uncovering and exploiting the potential of (oriented) electric fields to exert chemical catalysis and reaction control. *J Am Chem Soc.* 2020;142:12551-12562.
- Costentin C, Passard G, Robert M, Savéant J-M. Pendant Acid-Base Groups in Molecular catalysts: H-bond promoters or proton relays? Mechanisms of the conversion of CO₂ to CO by electrogenerated iron(0)porphyrins bearing prepositioned phenol functionalities. *J Am Chem Soc.* 2014;136:11821-11829.
- Fernández S, Franco F, Casadevall C, Martin-Diaconescu V, Luis JM, Lloret-Fillol J. A unified electro- and photocatalytic CO₂ to CO reduction mechanism with aminopyridine cobalt complexes. *J Am Chem Soc.* 2020;142:120-133.
- Cometto C, Chen L, Lo Po-K, et al. Highly selective molecular catalysts for the CO₂ -to-CO electrochemical conversion at very low overpotential. Contrasting Fe vs Co quaterpyridine complexes upon mechanistic studies. *ACS Catal.* 2018;8:3411-3417.
- Hammouche M, Lexa D, Momenteau M, Saveant JM. Chemical catalysis of electrochemical reactions. Homogeneous catalysis of the electrochemical reduction of carbon dioxide by iron("0") porphyrins. Role of the addition of magnesium cations. *J Am Chem Soc.* 1991;113:8455-8466.

37. Bhugun I, Lexa D, Savéant J-M. Catalysis of the electrochemical reduction of carbon dioxide by iron(0) porphyrins. Synergistic effect of Lewis acid cations. *J Phys Chem.* 1996;100:19981-19985.
38. Owensby DA, Parker AJ, Diggle JW. Solvation of ions. XXI. Solvation of potassium cation in nonaqueous solvents. *J Am Chem Soc.* 1974;96:2682-2688.
39. Mähler J, Persson I. A study of the hydration of the alkali metal ions in aqueous solution. *Inorg Chem.* 2012;51:425-438.
40. Bullock RM, Das AK, Appel AM. Surface immobilization of molecular electrocatalysts for energy conversion. *Chem - A Eur J.* 2017;23:7626-7641.
41. Sun L, Reddu V, Fisher AC, Wang X. Electrocatalytic reduction of carbon dioxide: opportunities with heterogeneous molecular catalysts. *Energy Environ Sci.* 2020;13:374-403.
42. Maurin A, Robert M. Catalytic CO₂ -to-CO conversion in water by covalently functionalized carbon nanotubes with a molecular iron catalyst. *Chem Commun.* 2016;52:12084-12087.
43. Rudnev AV, Zhumaev UE, Kuzume A, et al. The promoting effect of water on the electroreduction of CO₂ in acetonitrile. *Electrochim Acta.* 2016;189:38-44.
44. Moura De Salles Pupo M, Kortlever R. Electrolyte effects on the electrochemical reduction of CO₂. *ChemPhysChem.* 2019;20:2926-2935.
45. Nitopi S, Bertheussen E, Scott SB, et al. Progress and perspectives of electrochemical CO₂ reduction on copper in aqueous electrolyte. *Chem Rev.* 2019;119:7610-7672.
46. Mehara J, Roithová J. Identifying reactive intermediates by mass spectrometry. *Chem Sci.* 2020;11:11960-11972.
47. Liu J, Yu K, Zhang H, He J, Jiang J, Luo H. Mass spectrometric detection of fleeting neutral intermediates generated in electrochemical reactions. *Chem Sci.* 2021;12: 9494-9499.
48. Herl T, Matysik F-M. Recent developments in electrochemistry-mass spectrometry. *ChemElectroChem.* 2020;7:2498-2512.
49. Oberacher H, Pitterl F, Erb R, Plattner S. Mass spectrometric methods for monitoring redox processes in electrochemical cells. *Mass Spectrom Rev.* 2015;34:64-92.
50. Wang Z, Zhang Y, Liu B, et al. In situ mass spectrometric monitoring of the dynamic electrochemical process at the electrode-electrolyte interface: a SIMS approach. *Anal Chem.* 2017;89:960-965.
51. Miller TM. *Atomic, Molecular, and Optical Physics.* Elsevier Masson SAS; 2005.
52. Zins E-L, Pepe C, Schröder D. Energy-dependent dissociation of benzylpyridinium ions in an ion-trap mass spectrometer. *J Mass Spectrom.* 2010;45:1253-1260.
53. Rahrt R, Auth T, Demireva M, Armentrout PB, Koszinowski K. Benzhydrylpyridinium ions: a new class of thermometer ions for the characterization of electrospray-ionization mass spectrometers. *Anal Chem.* 2019;91:11703-11711.
54. Mondal B, Rana A, Sen P, Dey A. Intermediates involved in the 2e⁻/2H⁺ + reduction of CO₂ to CO by iron(0) porphyrin. *J Am Chem Soc.* 2015;137:11214-11217.
55. Costentin C, Drouet S, Passard G, Robert M, Savéant J-M. Proton-coupled electron transfer cleavage of heavy-atom bonds in electrocatalytic processes. Cleavage of a C-O bond in the catalyzed electrochemical reduction of CO₂. *J Am Chem Soc.* 2013;135:9023-9031.
56. Fukuzumi S, Lee Y-M, Ahn HS, Nam W. Mechanisms of catalytic reduction of CO₂ with heme and nonheme metal complexes. *Chem Sci.* 2018;9:6017-6034.
57. Schwarz H, Asmis KR. Identification of active sites and structural characterization of reactive ionic intermediates by cryogenic ion trap vibrational spectroscopy. *Chem - A Eur J.* 2019;25:2112-2126.
58. Roithová J, Gray A, Andris E, Jašík J, Gerlich D. Helium tagging infrared photodissociation spectroscopy of reactive ions. *Acc Chem Res.* 2016;49:223-230.
59. Jašík J, Žabka J, Roithová J, Gerlich D. Infrared spectroscopy of trapped molecular dications below 4K. *Int J Mass Spectrom.* 2013;354-355:204-210.
60. Menges FS, Craig SM, Tötsch N, et al. Capture of CO₂ by a cationic nickel(II) complex in the gas phase and characterization of the bound, activated CO₂ molecule by cryogenic ion vibrational predissociation spectroscopy. *Angew Chem Int Ed.* 2016;55:1282-1285.
61. Iskra A, Gentleman AS, Cunningham EM, Mackenzie SR. Carbon dioxide binding to metal oxides: Infrared spectroscopy of NbO₂+(CO₂) and TaO₂+(CO₂) complexes. *Int J Mass Spectrom.* 2019;435:93-100.
62. Dodson LG, Thompson MC, Weber JM. Characterization of intermediate oxidation states in CO₂ activation. *Annu Rev Phys Chem.* 2018;69:231-252.
63. Amanullah Sk, Saha P, Dey A. Activating the Fe(I) state of iron porphyrinoid with second-sphere proton transfer residues for selective reduction of CO₂ to HCOOH via Fe(III/II)-COOH intermediate(s). *J Am Chem Soc.* 2021;143:13579-13592.
64. Römelt C, Song J, Tarrago M, et al. Electronic structure of a formal iron(0) porphyrin complex relevant to CO₂ reduction. *Inorg Chem.* 2017;56:4745-4750.
65. Davethu PA, De Visser SP. CO₂ reduction on an iron-porphyrin center: a computational study. *J Phys Chem A.* 2019;123:6527-6535.
66. Monteiro MCO, Dattila F, Hagedoorn B, García-Muelas R, López N, Koper MTM., Absence of CO₂ electroreduction on copper, gold and silver electrodes without metal cations in solution. *Nat Catal.* 2021;4:654-662.
67. Gilissen PJ, Swartjes A, Spierenburg B, et al. Rapid and scalable synthesis of chiral porphyrin cage compounds. *Tetrahedron.* 2019;75:4640-4647.
68. Gerlich D, Jašík J, Roithová J. Tagging fullerene ions with helium in a cryogenic quadrupole trap. *Int J Mass Spectrom.* 2019;438:78-86.
69. Zhao Y, Truhlar DG. A new local density functional for main-group thermochemistry, transition metal bonding, thermochemical kinetics, and noncovalent interactions. *J Chem Phys.* 2006;125:194101.
70. Grimme S, Antony J, Ehrlich S, Krieg H. A consistent and accurate ab initio parametrization of density functional dispersion correction (DFT-D) for the 94 elements H-Pu. *J Chem Phys.* 2010;132:154104.
71. Weigend F, Ahlrichs R. Balanced basis sets of split valence, triple zeta valence and quadruple zeta valence quality for H to Rn: design and assessment of accuracy. *Phys Chem Chem Phys.* 2005;7:3297-3305.
72. Becke AD. Density-functional thermochemistry. III. The role of exact exchange. *J Chem Phys.* 1993;98:5648-5652.
73. Lee C, Yang W, Parr RG. Development of the Colle-Salvetti correlation-energy formula into a functional of the electron density. *Phys Rev B.* 1988;37:785-789.
74. Miehlich B, Savin A, Stoll H, Preuss H. Results obtained with the correlation energy density functionals of Becke and Lee, Yang and Parr. *Chem Phys Lett.* 1989;157:200-206.

SUPPORTING INFORMATION

Additional supporting information can be found online in the Supporting Information section at the end of this article.

How to cite this article: Surendran AK, Tripodi GL, Pluhařová E, et al. Host-guest tuning of the CO₂ reduction activity of an iron porphyrin cage. *Nat Sci.* 2023;3:e20220019. <https://doi.org/10.1002/ntls.20220019>